Volume 16
Number 4
28 January 2025
Pages 389-504

Polymer Chemistry

rsc.li/polymers

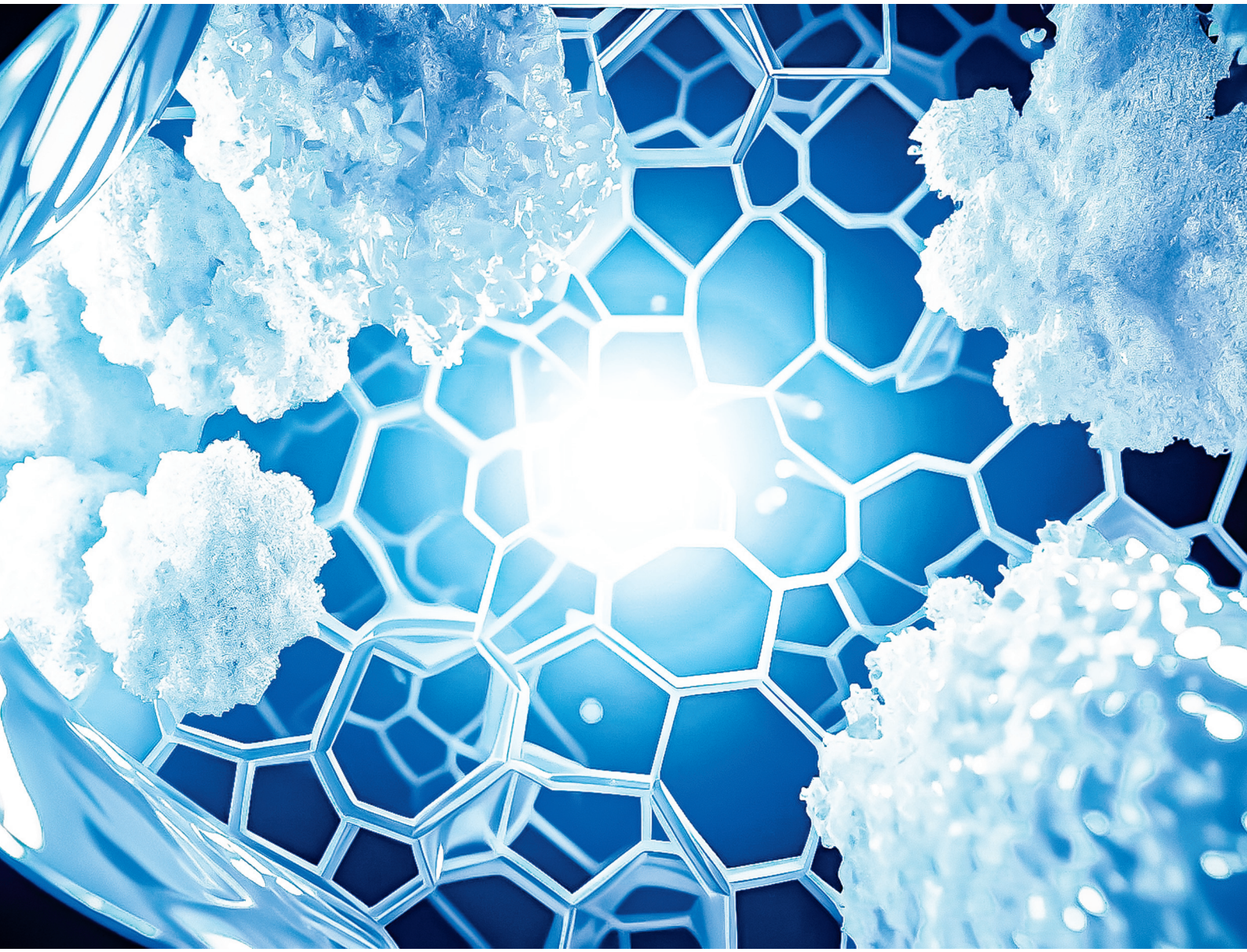

ISSN 1759-9962

ROYAL SOCIETY OF CHEMISTRY

PAPER
Shiao-Wei Kuo *et al.*
Rational decoration of porous organic polymers with silver nanoparticles for strategic reduction of hazardous nitroaryl compounds

15 YEARS ANNIVERSARY

Polymer Chemistry

ROYAL SOCIETY OF CHEMISTRY

PAPER

View Article Online
View Journal | View Issue

Cite this: *Polym. Chem.*, 2025, **16**, 422

Rational decoration of porous organic polymers with silver nanoparticles for strategic reduction of hazardous nitroaryl compounds†

Mohammed G. Kotp,[a] Ahmed F. M. EL-Mahdy [a] and Shiao-Wei Kuo *[a,b]

Porous organic polymers (POPs) have garnered significant attention across various industries due to their promising physicochemical properties. In this study, we employ the classical Friedel–Crafts alkylation strategy to synthesize two types of porous organic polymers, namely Py–CH POP and TPA–CH POP, utilizing chloranil (CH), pyrene (Py), and triphenylamine (TPA) as building blocks. The Py–CH POP exhibits coaxial-like morphologies, uniform micropores, and a moderate surface area of up to 822 m^2 g^{-1}, along with excellent thermal stability, recording a char output of 69.6 wt%. Notably, these CH POPs contain dynamic hydroxyl groups that can effectively attract Ag^+ ions from silver nitrate solutions and facilitate their reduction into silver nanoparticles, resulting in the formation of Ag@Py–CH and Ag@TPA–CH POP nanocomposites. These nanocomposites serve as efficient nano-catalysts for the reduction of hazardous *p*-nitrophenol (*p*-NP) to the safer *p*-aminophenol (*p*-AP) at ambient temperature. Importantly, the Ag@Py–CH and Ag@TPA–CH POP nanocomposites demonstrate comparable normalized reduction rates of *p*-NP, reaching up to 65.3 mg s^{-1}. The quaternary amine sites in the Ag@TPA–CH POP nanocomposites play a crucial role in this catalytic reaction, enhancing interactions with the phenolic hydroxyl groups of *p*-NP and thereby accelerating the reduction process compared to Ag@Py–CH POP. This strategy presents a dynamic approach for the reduction of *p*-NP, leading to the clean production of *p*-AP.

Received 21st October 2024,
Accepted 11th November 2024

DOI: 10.1039/d4py01179a

rsc.li/polymers

Introduction

Nitroaromatic compounds are of significant interest due to their widespread use in various industries, including the production of dyes, pesticides, and pharmaceuticals. However, their extensive application has led to severe environmental contamination, as these compounds are highly toxic, recalcitrant to biodegradation, and pose serious risks to human health and ecosystems. The electron-withdrawing nature of the nitro group contributes to their chemical stability and resistance to degradation, making them persistent pollutants in soil and groundwater thus chief calls are derived for their elimination.[1–3] Realistically, herbicides and dyes industries generate vast amounts of hazardous nitroaromatic molecule, called *p*-nitrophenol (*p*-NP), as its cumulation, propagation out of food chain and within nervous system respectively can give rise to failure of liver and kidney in addition to other lethal diseases.[4,5] Therefore, Environmental Protection Agency (EPA) has classified *p*-NP as a dangerous toxin then maximizes content of it to 10 parts per billion (ppb) within drinkable aqua. Indeed, there are numerous methods recommended to serve the elimination of *p*-NP such as microwave-assisted oxidation,[6] bacterial remediation, gamma irradiation,[7] electro,[8] or photocatalytic oxidations, photocatalytic ozonation,[9] and reductions; however, these disposing methods have considerable defects. For example, elevated operational costs as well as unsafety of electrical pulses and gamma rays of microwave-electrochemical utilizes oxidations techniques preclude the practical uses of these methods.[10] The photocatalytic degradation bounds by faint concentrations.[11] Bacterial remediation can be employed for limiting the *p*-NP content (<200 mg L^{-1}), besides each form of nitroaryls acquires a certain kind of bacterium.[12] On the other hand, the heterogenous ozonation able to degrade *p*-NP but suffers unsustainability and an instability after consecutive cycles.[13]

Importantly, heterogeneous reductions of nitrophenols consider the proper strategy due to cheaper energy requirements, effectiveness, ease of operation, and security, nevertheless, higher reduction rates are still industrial provocations.[1,14] On the other hand, reducing the nitro units is a vital process toward removal these hazardous part; moreover, *para*-aminophenol (*p*-AP) molecule affording through this reaction, con-

[a]*Department of Materials and Optoelectronic Science, Center for Functional Polymers and Supramolecular Materials, National Sun Yat-Sen University, Kaohsiung, 80424, Taiwan. E-mail: kuosw@faculty.nsysu.edu.tw*
[b]*Department of Medicinal and Applied Chemistry, Kaohsiung Medical University, Kaohsiung 807, Taiwan*

† Electronic supplementary information (ESI) available. See DOI: https://doi.org/10.1039/d4py01179a

siders safe and applicable for many industries as drugs, anticorrosion materials, dyes,[15] as well as an optoelectronic molecule for such synthesis of phenolic resin,[16–18] polybenzoxazine,[19] and poly(cyanate ester).[20] Interestingly, the rate of *p*-NP reduction accelerates using few quantities of energy to fulfil the H_2 pressure. On the other hand, such reducing the kinetic barrier of reducing agents toward electron acceptors fasts the corresponding reduction rate of *p*-NP.

Recently, noble metals nanoparticles (Pt, Ag, Pd, Ru, and Au) albeit generally expensive are employ as beneficial catalysts for such these reductions processes.[21–24] Considering this important point, Ag is cost effective, thermally stable, and comparatively abundant relative to other noble metals.

Otherwise, Ag nanoparticles could suffer from agglomeration thus, chemists challenges to anchor these nanoparticles onto diverse carriers such as silica substrates,[25] carbonaceous materials,[26] or inorganic materials to limit their severe self-assembly and suite the proper application.[24,27] Notably, Ag nanoparticles have diverse applications across multiple industries. They serve as antimicrobial agents in medical devices and wound dressings, help inhibit microbial growth in food packaging and play a role in water purification for environmental remediation. Additionally, Ag nanoparticles are utilized in electronics for conductive inks and sensors, in cosmetics for their antimicrobial benefits, in textiles for antibacterial protection, and in biosensors for detecting biological molecules.

Porous organic polymers (POPs) have engaged great concern owing to their unparalleled features such as high thermal and chemical stabilities, high surface area, lower density and diversified synthetic styles.[28–44] Actually, the synthesis cost of POPs considers a potential defect of their use due to catalyzing their polymerization processes *via* expensive metal complexes.[45] For example; cobalt complexes catalyzes the trimerizations of alkynes,[46] Ni-catalyzed Yamamoto homocoupling,[47] and Pd-catalyzes Suzuki reactions[48–52] or Sonogashira–Hagihara couplings.[39,53,54] Otherwise, hypercrosslinked polymers (HCPs) could be synthesized through simple and cost-effective materials *via* Friedel–Crafts alkylation catalyzes cost effective ferric chloride ($FeCl_3$) without uses of functionalized monomers or precious metals.[55] Further, $FeCl_3$ can be drained completely after a simple workup. Furthermore, features derived monomers could likely to be fully kept as well as structures of obtained polymers can be characterized easily thus this strategy considers for prospective synthesis of POPs.[56]

While it is true that previous studies have utilized reducing agents such as hydrazine for synthesizing Ag nanoparticles onto POPs, our work diverges by exploring alternative simple and green reduction methods. Notably, the distinct properties of pyrene (Py) and triphenylamine (TPA) linked chloranil (CH) in the reduction of nitroaromatic compounds have not been thoroughly investigated in prior research. Moreover, green reduction of Ag nanoparticles onto POPs is still challengeable. This exploration is crucial, as it may lead to novel insights into the synthesis and functionality of Ag nanoparticles in environmental applications. Our study aims to contribute valuable knowledge to the field and enhance the understanding of how different monomers can impact the efficiency and effectiveness of decorated Ag nanoparticles in conjunction with POPs for environmental remediation.

Herein, we synthesized a couple of POPs nominated Py–CH and TPA–CH POPs based Py and TPA respectively with CH for the first time considering Friedel–Crafts alkylation strategy (Scheme 1). Those Py–CH and TPA–CH POPs possessed high surface area up to 463, and 822 $m^2\ g^{-1}$, respectively, with higher thermal stabilities. Truly, CH considers as a strong oxidizing agent thus their Keto groups can be easily converted into hydroxyl groups, consequently, our Py–CH and TPA–CH POPs could offer many hydroxyl sites.[57] Fulfilling the concept of green chemistry, the generated hydroxyl groups within CH POPs able to deal as chelating and reductive sites for Ag^+ ions into Ag nanoparticles without using of any external and hazardous reducing agents such as hydrazine affording Ag@Py–CH POP, and Ag@TPA–CH POP nanocomposites, respectively.

We performed a rational synthesis of Ag decorated POPs using various aqueous concentrations of silver salt (1 and 3 mM) for each CH POPs affording 1Ag@Py–CH POP, 3Ag@Py–CH POP, 1Ag@TPA–CH POP and 3Ag@TPA–CH POP. The catalysis reactions using 1Ag@Py–CH POP, 3Ag@Py–CH POP, 1Ag@TPA–CH POP and 3Ag@TPA–CH POP nanocomposites toward the reduction of *p*-NP achieving pseudo first order kinetic model with higher catalysis rates up to 4.03×10^{-3}, 9.7×10^{-3}, 6.34×10^{-3}, and $6.34 \times 10^{-3}\ s^{-1}$ respectively. Furthermore, our decorated CH POPs showed comparable normalized kinetic rates regarding previous catalysts.

Experimental

Materials

Reagents including anhydrous ferric chloride ($FeCl_3$) and dichloroethane (DCE, 99%) were purchased from Sigma Aldrich. Triphenylamine (TPA, powder), and silver nitrate ($AgNO_3$, crystals) were supported by Alfa Aesar. Chloranil (CH, powder), *p*-NP was obtained from TCI America. All solvents used for achieving our study were from Analytical quality utilized without any additional purifying.

Preparation of pristine Py–CH POP

The Friedel–Crafts alkylation protocol was reported previously.[55] Briefly, Py (4 mmol, 0.81 g) and anhydrous $FeCl_3$ (0.012 mmol, 1.97 g) were dissolved in anhydrous 1,2-dichloroethane (50 mL), then chloranil powder (4.1 mmol, 1 g) was added to the reaction flask. The mixture was magnetically stirred under reflux system and nitrogen atmosphere for ten consecutive hours at ambient temperature, subsequently rising at 100 °C for 4 days. During this process, the elastic precipitate was separated out. The reaction mixture has poured into methanol for recrystallization then washed by water, methanol, acetone, and THF to eliminate any salt residuals. Collect the powder by filtration, then dried by suction at 100 °C for a full day (yield: 85%).

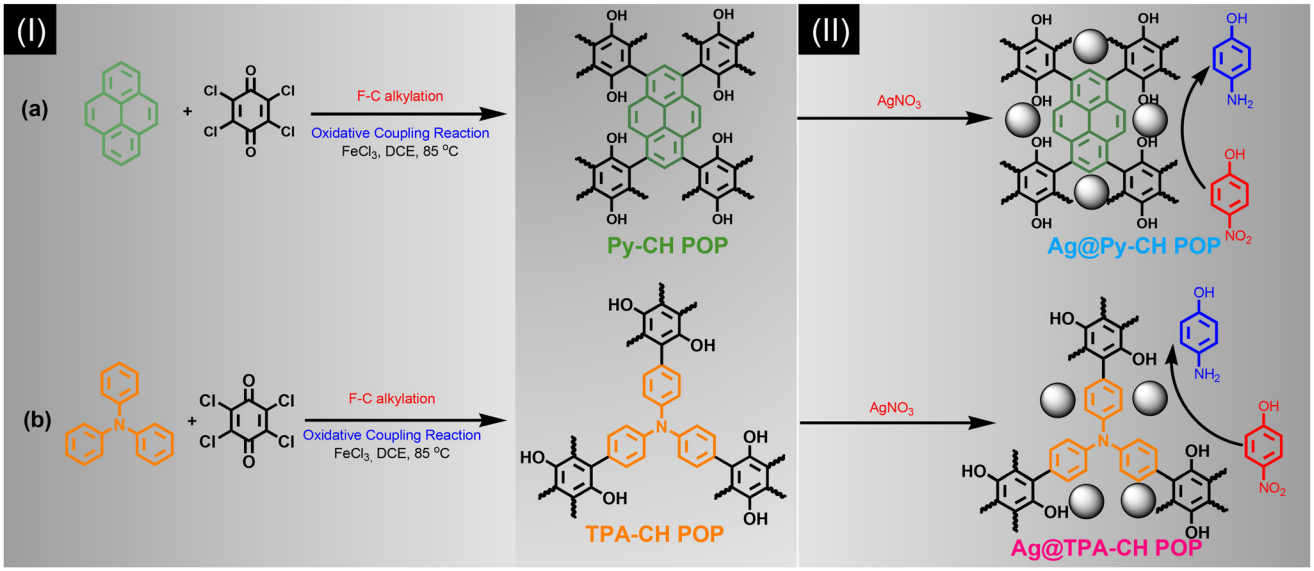

Scheme 1 Synthesis of (Ia) Py–CH POP, (Ib) TPA–CH POP, (IIa) Ag@Py–CH POP and (IIb) Ag@TPA–CH POP nanocomposites.

Preparation of TPA–CH POP

TPA (4.1 mmol, 0.98 g) with dehydrated $FeCl_3$ (1.97 g, 0.012 mmol) had dissolved in anhydrous 1,2-dichloroehtane (50 mL), then chloranil (4.1 mmol, 1 g) was supplemented to reaction mixture. The mixture was magnetically stirred under same previously mentioned conditions about ten consecutive hours at ambient conditions then temperature had raised as high as 100 °C for 4 days. During this process, the elastic precipitate was filtered out. The reaction mixture has poured into methanol for recrystallization then washed by water, methanol, acetone, and THF to eliminate any salt residuals. Finally, the greenish-yellow powder had been retrieved and processed by suction at 100 °C for 24 h (yield: 93%).

Preparation of Ag@Py–CH and Ag@TPA–CH POPs nanocomposites

The green strategy of anchoring Ag nanoparticles has previously discussed.[58] A couple of $AgNO_3$ fluids were made individually by concentration 0.1 and 0.3 mM. The Py–CH and TPA–CH POPs (10 mg) were immersed in the specific $AgNO_3$ fluids (10 mL). The combinations were swirled magnetically overnight, then powders were separated, washed up to five times using methanol and water. Powders were filtered, then dried out under 50 °C producing outcomes of *x*Ag@Py–CH and *x*Ag@TPA–CH POPs nanocomposites where *x* was 1 or 3 depending on the corresponding concentration of $AgNO_3$. ICP detected 0.67, 1.20, 0.29, and 0.58 wt% of Ag respectively for 1Ag@Py–CH POP, 3Ag@Py–CH POP, 1Ag@TPA–CH POP and 3Ag@TPA–CH POP.

Conversion from *p*-NP into *p*-AP mediated Ag@Py–CH POP nanocomposite

The reduction procedures of *p*-NP has reported previously.[4,23] Briefly, *p*-NP (2.0 mL, 0.16 mM) plus $NaBH_4$ (0.5 mL, 0.08 M) had been charged into the well stoppered chamber, afterward previously *x*Ag@Py–CH or *x*Ag@TPA–CH POPs nanocomposites (0.2 mL, 1 mg mL^{-1}) were charged. Notably, similar concentrations regarding the *p*-NP were employed within conditions of reduction experiments. Moreover, a UV-Vis spectrophotometer was employed to monitor the progress of the reduction over time intervals.

Recovery of Ag@Py–CH and Ag@TPA–CH POPs nanocomposites

To define recovery processes of 1Ag@Py–CH and 1Ag@TPA–CH POPs nanocomposites toward such conversion of the *p*-NP, nanocomposites quantities (catalyst) were increased tenfold to minimize error effect. The Ag@Py–CH and Ag@TPA–CH POP nanocomposites were conducted for five consecutive runs; they were separated through centrifugation at 6000 rpm then washed by water and methanol, dried before the subsequent run as well.

Results and discussion

Characterizations of CH POPs

Couple novel CH-based POPs nominated Py–CH and TPA–CH POPs were synthesized in a quantitative yield *via* Friedel–Crafts alkylation strategy between (CH) and two aromatic units Py and TPA, respectively (Scheme I(a) and II(b)). Importantly, both CH POPs do not show any solubility through standard solvents including acetone, EtOH, MeOH, or even THF, implying their high degree of crosslinking. The chemical textures of as-prepared CH-POPs were clarified applying FTIR as well solid state ^{13}C spinning (MAS) NMR scans. Initially, the FTIR profiles of Py–CH and TPA–CH POPs, as shown in Fig. 1(a), demonstrate the complete disappearance of strong peaks

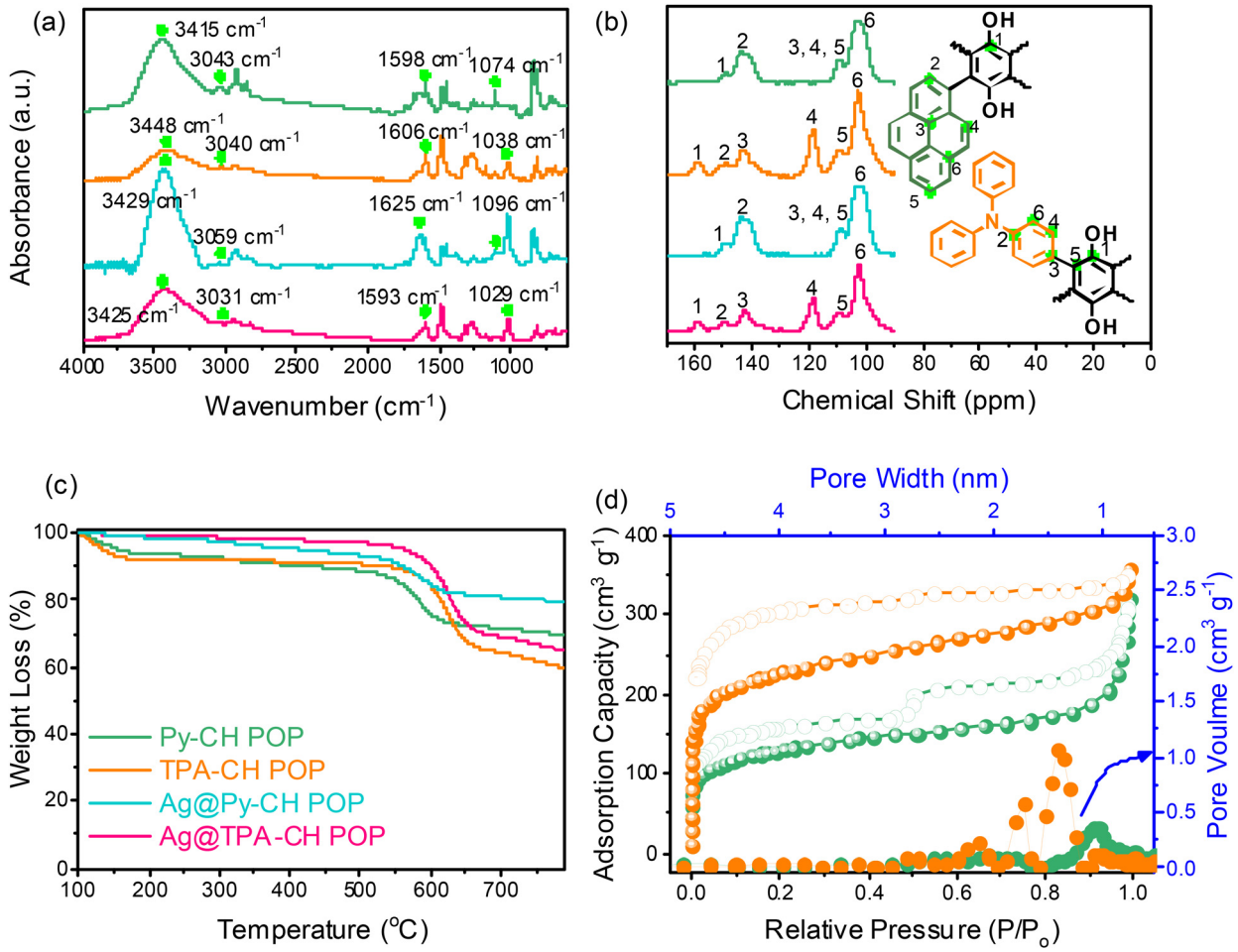

Fig. 1 (a) FTIR, (b) sold state NMR (c) TGA profiles of Py–CH, TPA–CH, Ag@Py–CH, and Ag@TPA–CH POPs, and (d) BET and pore sizes profile of Py–CH, and TPA–CH POPs.

around 600 cm^{-1}, which correspond to vibrational C–Cl units. This observation confirms the successful crosslinking between the building subunits. The FTIR spectrum of Py–CH displays characteristic signals at 3415 cm^{-1}, 3043 cm^{-1}, 1598 cm^{-1}, and 1074 cm^{-1}, while TPA–CH POP exhibits bands at approximately 3448 cm^{-1}, 3040 cm^{-1}, 1606 cm^{-1}, and 1038 cm^{-1}. These peaks are attributed to the vibrational modes of C-OH, C–H (aromatic), C=C, and C–O, respectively, indicating successful formation of CH-POPs.

In the ^{13}C SSNMR spectrum of Py–CH POP (Fig. 1(b)), a peak at 148.211 ppm is attributed to the carbon atom connected to hydroxyl (OH) groups. Additionally, peaks observed at 143.676 ppm, 109.052 ppm, and 102.241 ppm correspond to the aromatic C=C and C–H bonds present in the polymer structure. Conversely, ^{13}C SSNMR spectrum of TPA–CH POP (Fig. 1(b)) exhibits a signal at 157.867 ppm, which is assigned to the carbon attached to an OH group, along with a peak at 149.565 ppm corresponding to the C–N bond in the TPA monomer. Further peaks at 143.109 ppm, 118.205 ppm, 109.904 ppm, and 102.525 ppm are associated with the aromatic C=C and C–H bonds in TPA–CH POP.

For better emphasizing the elemental composition of CH-POPs surfaces and their relative electronic states we conducted XPS analysis (Fig. S1(a) and (b)†). In this regard, the high resolution XPS signals of C 1s, O 1s, and N 1s were clearly detected for Py–CH and TPA–CH POPs materials (Fig. 2), which primarily confirms their chemical texture. Further, the C 1s spectrum of Py–CH POP sample deconvolutes into three signals (Fig. 2a), which impute to triple carbonaceous species, including sp^2 carbons (C=C, 284.9 eV), sp^2 carbon attached phenolic O (C-OH, 286.2 eV), C=O units (287.3 eV). Moreover, deconvolutions of this O signal in Py–CH POP sample exhibit three oxygen species assigned at 534.4, 533.4, 532.1 eV (Fig. 2(a)), which respectively reveals to Waterous O, C-OH, as well –C=O units. Otherwise, C 1s profile within TPA–CH POP sample deconvolutes into four signals (Fig. 2(b)) referring to four carbonaceous species, including sp^2 carbons (C=C, 284.8 eV), sp^2 carbon attached phenolic oxygen (C-OH, 285.9 eV), sp^2 carbon (C–N, 286.3 eV), as well as C=O groups (287.1 eV).

Similar to Py–CH POP, the TPA–CH POP sample shows triple oxygen species at around 534.4, 533.5, and 532.2 eV (Fig. 2b), respectively reveals to hydrated O, C-OH, as well as

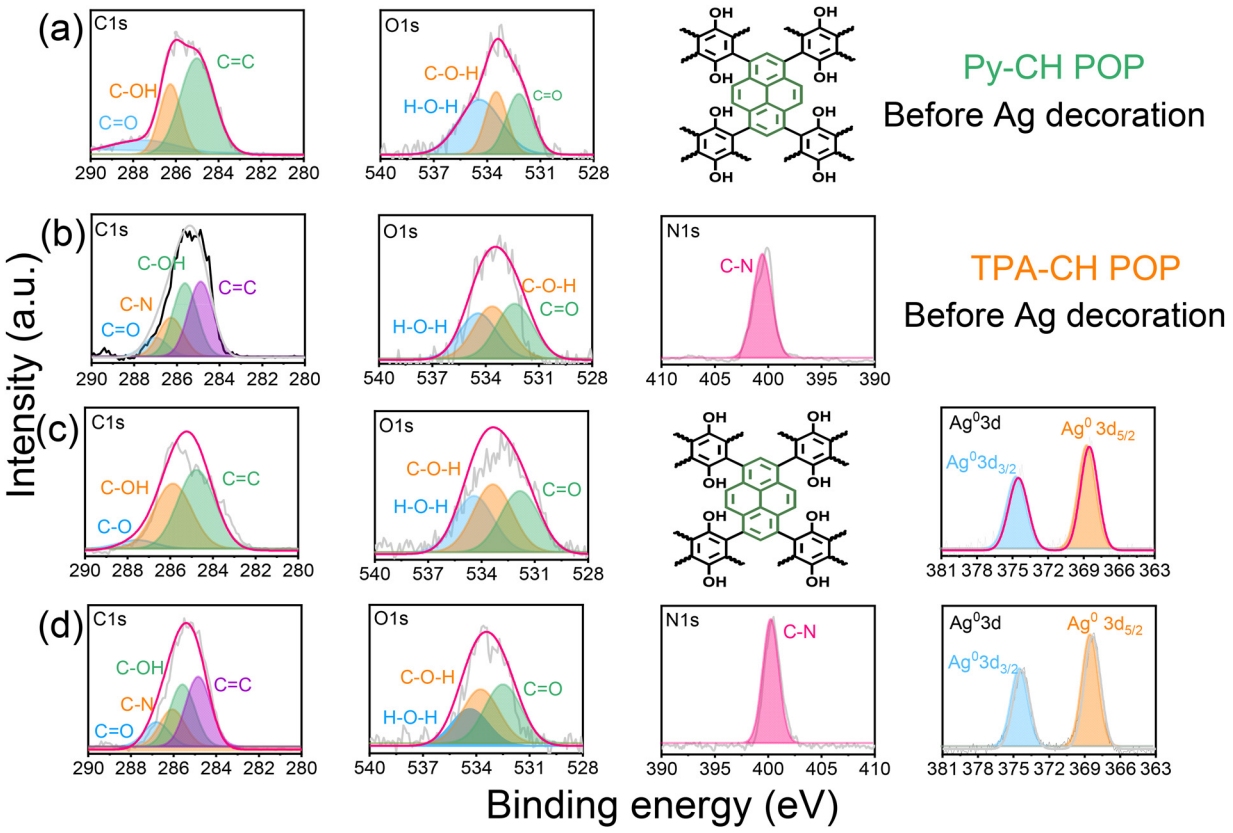

Fig. 2 XPS spectrum profiles of Py–CH (row a), TPA–CH (row b) POPs, 3Ag@Py–CH (row c), and 3Ag@TPA–CH POPs (row d).

–C=O units. Importantly, XPS profile of TPA–CH POP (Fig. 2(b)) shows an additional N 1s signal which fits to singlet peak at 400.1 eV of C–N units. Actually, POPs are renowned for their high thermal stabilities, in this regard, both Py–CH, and TPA–CH POPs exhibit outstanding degree of thermal stabilities based TGA under an inert condition. As emphasized in Fig. 1c, as well Table S1,† the decomposition temperatures (T_{d10}) of Py–CH, and TPA–CH POPs are 437 and 540 °C respectively, achieving high char yields of 69.6 wt% and 59.8 wt%, respectively. These outstanding thermal stabilities of Py–CH, and TPA–CH POPs confirm the high degree of π–π stacking interactions between their layers. Porosities of as-synthesized CH POPs were characterized though analyzing N_2 adsorb/desorb isotherms under 77 K (Fig. 1(d)). These plots display an acute increase under minimal relative pressure emphasizing their microporous nature (Fig. 1(d)), in addition to high specific surface areas which reached up to 463 and 822 $m^2\ g^{-1}$ for Py–CH, and TPA–CH POPs, respectively (Fig. 1(d) and Table S1†), and these surface areas fall within a moderate range when compared to state-of-the-art porous materials.[4,59] Interestingly, the sharp desorption stage occurred in between P/P_0 of 0.5 to 0.45 reveals the cavitation of N_2 elucidating these pores possess the geometry of an inkbottle.[60,61] Moreover, nonlocal density functional theory (NLDFT) confirmed the micrporous nature of Py–CH and TPA–CH POPs elucidating their tunable pore sizes of 1.07, and 1.34 nm respectively. Pore volumes of those Py–CH and TPA–CH POPs were 0.492 and 0.547 $cm^3\ g^{-1}$ respectively (Table S1†). Motivated by physical properties, chemical nature and high surface areas of Py–CH, and TPA–CH POPs, they assume to be potential surfaces for noble metals decoration.

The morphologies of Py–CH, and TPA–CH POPs were visualized using these spectroscopies of FE-SEM and HR-TEM. As shown in Fig. 3(a) and (b), FE-SEM images imply that both Py–CH and TPA–CH POPs exhibit coaxial structures. Basically, TEM image (Fig. 3c) shows hollow tubes of Py–CH POP, and nanorods like structures of TPA–CH POP. This coaxial natures may reveal to non-planar structure of CH molecule within these POPs.[62,63]

Characterizations of Ag@CH POPs

In this section, we conducted a green embellishment (no dangerous reducing chemicals) to get Ag@CH POPs. Importantly, the Ag^+ ions assumed to be captured through impregnated hydroxyl units of Py–CH, and TPA–CH POPs (Scheme 1II).[58] These hydroxyl (OH) units not only capture Ag^+ but also facilitate the reduction of Ag^+ ions to yield Ag nanoparticles and thus this study offers a green methodology.

The FTIR spectra of the Ag@Py–CH and Ag@TPA–CH POP nanocomposites, also displayed in Fig. 1(a), show only slight shifts in signals compared to the pristine Py–CH and TPA–CH POPs. Specifically, the vibrational modes for Ag@Py–CH POP

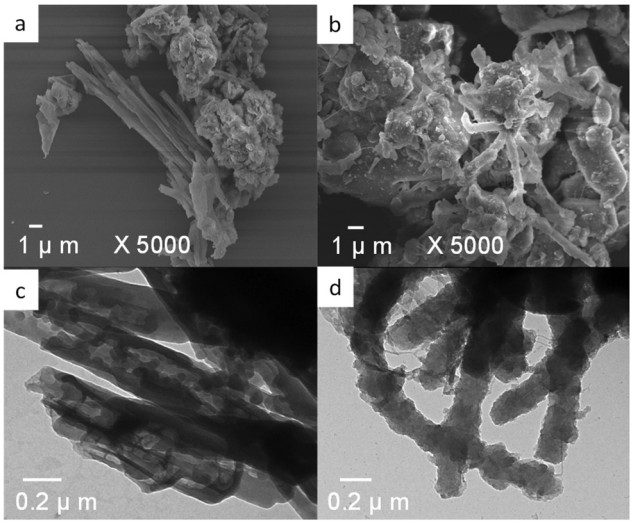

Fig. 3 (a and b) SEM and (c and d) TEM images of Py–CH POP, as well TPA–CH POP.

are observed at 3429 cm^{-1}, 3059 cm^{-1}, 1625 cm^{-1}, and 1096 cm^{-1}. Similarly, for Ag@TPA–CH POPs, the shifts occur at 3425 cm^{-1}, 3431 cm^{-1}, 1593 cm^{-1}, and 1029 cm^{-1}. These results further support our findings regarding the physical interactions between silver nanoparticles and the surfaces of CH-POPs. Similarly, the ^{13}C SSNMR spectra of the as-decorated nanocomposites Ag@Py–CH and Ag@TPA–CH POPs, as illustrated in Fig. 1(b), exhibit subtle chemical shifts compared to the pristine Py–CH and TPA–CH POPs. These shifts provide further confirmation of the previously mentioned assumption regarding the physical interactions between the Ag nanoparticles and the surfaces of the CH-POPs. Importantly, TGA of 3Ag@Py–CH, and 3Ag@TPA–CH POPs nanocomposites showed slightly higher T_{d10} values than pristine Py–CH, and TPA–CH POPs, which raised up to 563, and 602 °C, respectively. Furthermore, Ag@Py–CH, and Ag@TPA–CH POPs nanocomposites achieved a high char yields up to 65.0, and 79.5 wt%, respectively as shown in Fig. 1(c). To validate the thermal properties of our Ag nanocomposites, we have conducted TGA for both the pristine Py–CH POP and Ag@Py–CH POP in an air atmosphere. The results indicate a char yield of 1.11% for the pristine Py–CH POP and 2.07% for the Ag@Py–CH POP after heating to 800 °C. Additionally, the T_{d10} were found to be 352 °C for the pristine Py–CH POP and 525 °C for the Ag@Py–CH POP (Fig. S2†). Similarly, we performed TGA on the pristine TPA–CH POP and Ag@TPA–CH POP, which yielded char yields of 0.66% and 1.26%, respectively. The T_{d10} values were recorded at 510 °C for the pristine TPA–CH POP and 521 °C for the Ag@TPA–CH POP. These inspiring TGA results imply the high thermal stability of our nanocomposites (Ag@Py–CH, and Ag@TPA–CH POPs) after Ag decoration.

Fig. 4(a)–(d) show SEM visualizations of 1Ag@Py–CH, 3Ag@Py–CH, 1Ag@TPA–CH, and 3Ag@TPA–CH POPs nanocomposites respectively similar to their pristine surface Py–CH and TPA–CH POPs without severe Ag nanoparticles aggregations. On the other hand, Fig. 4(e) and (f) represent TEM images of 1Ag@Py–CH, and 3Ag@Py–CH POPs nanocomposites, confirming their hollow tubes like morphology with dispersed Ag nanoparticles without considerable agglomeration which reveals to their surface area as well as suitable pores within pristine Py–CH POP. Furthermore, the TEM visualizations of 1Ag@TPA–CH, and 3Ag@TPA–CH POPs nanocomposites (Fig. 4(g) and (h)) showed the good dispersibility of Ag nanoparticles onto rods of the TPA–CH POP. High resolution TEM (HR-TEM) employed for deeply visualizations of Ag nanoparticles deposited onto CH-POPs (Fig. 4(i)–(l)); interplanar distances between strips evaluated from corresponding lattice fringes of Ag@CH POPs nanocomposite to be 0.25 nm which matched well with lattice axis [111] of cubic Ag.[64] Furthermore, we conducted high resolution XPS survey, which confirm surface ingredients of 3Ag@Py–CH, and 3Ag@TPA–CH POPs nanocomposites (Fig. 2(c) and (d)). Actually, XPS analysis of 3Ag@Py–CH, and 3Ag@TPA–CH POPs nanocomposites exhibit the same functional groups of C 1s, O 1s, and N 1s of the pristine Py–CH, and TPA–CH POPs at the same binding energies. On the other hand, XPS analyses of 3Ag@Py–CH, and 3Ag@TPA–CH POPs nanocomposites (Fig. 2(c) and (d)) showed characteristic peaks of Ag atoms at binding energies of 374.9 eV (3d3/2) as well as 367.1 eV (3d5/2), respectively. Herein, we can assume that Ag nanoparticles could not effectively influence binding energies in those atomic ingredients of the pristine Py–CH, and TPA–CH POPs, this assumption matches well with FTIR results.

Catalytic reduction of *p*-NP

As early reported, the heterogeneous reduction of toxic nitrophenol into safer amine form considers the ideal disposal protocol due to chemical and bio stabilities of the former.[14,65] Basically, the catalytic conversion of *p*-NP into *p*-AP was selected as a model to investigate the catalytic efficiency of the synthesized Ag nanoparticles decorated POPs. Technically, aqueous $NaBH_4$ employs for reducing the *p*-NP into *p*-AP catalyzing *via* noble metals nanoparticles.[66,67] Firstly, the color of the *p*-NP converted to deep yellow upon the addition of $NaBH_4$ and the UV-Vis absorption peak of the former transformed from 317 nm into 400 nm as shown in Fig. 5(a)–(d), indicating the formation of *p*-NP^- anions.[68] Ultimately, color fades from deep yellow to ultimate colorless within time after the addition *x*Ag@Py–CH and *x*Ag@TPA–CH POPs nanocomposites (Fig. 5(a)–(d)). Therefore, the UV absorption signal at 400 nm decrease within time intervals in addition to generation another signal at 300 nm elucidating the conversion into *p*-AP and such complete disappearance of the former implies the complete reduction of *p*-NP.[69] Of note, no signal change was observed in the absence of our nano-catalysts within the same reaction, which validate the catalytic performances of *x*Ag@Py–CH and *x*Ag@TPA–CH POPs nanocomposites (Fig. S3(a) and (b)†).

Utilization of 1Ag@Py–CH, 3Ag@Py–CH, 1Ag@TPA–CH and 3Ag@TPA–CH POPs nanocomposites, derived to complete

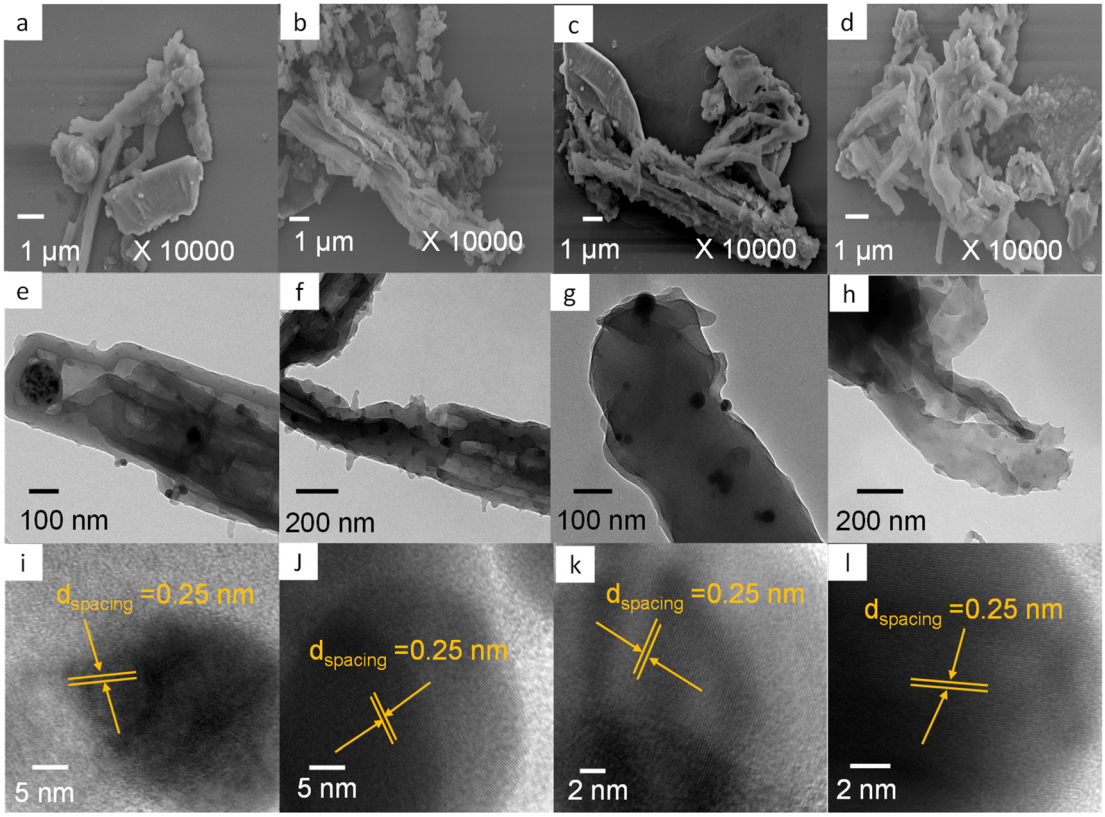

Fig. 4 (a–d) SEM images of (a) 1Ag@Py–CH POP, (b) 3Ag@Py–CH POP, (c) 1Ag@TPA–CH POP, (d) 3Ag@TPA–CH POP (d), (e–h) TEM and (i–l) HR-TEM images of (e and i) 1Ag@Py–CH POP, (f and j) 3Ag@Py–CH POP, (g and k) 1Ag@TPA–CH PO, and (h and l) 3Ag@TPA–CH POP.

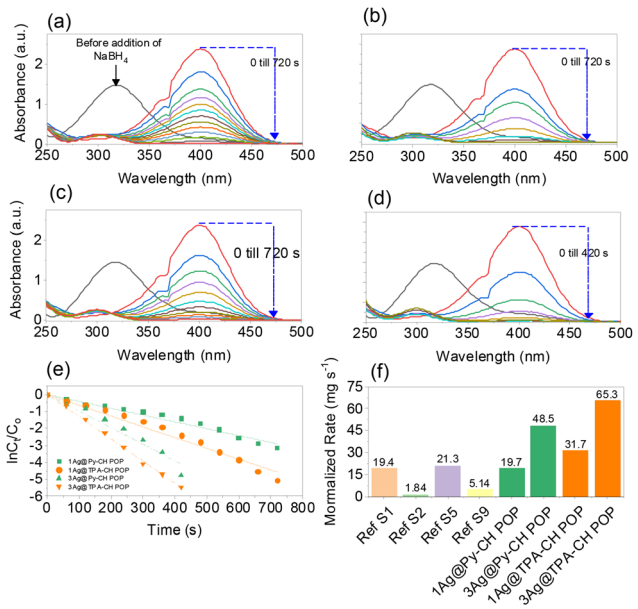

Fig. 5 UV-Visible profiles of 1Ag@Py–CH POP (a), 3Ag@Py–CH POP (b), 1Ag@TPA–CH POP (c), 3Ag@TPA–CH POP (d) within reduction of *p*-NP, pseudo first order kinetic assumptions of *p*-NP reduction using CH-POPs nanocomposites (e) and comparing of reduction normalized rates of CH-POPs with reported catalysts (f).

reductions of *p*-NP within 660, 360, 480, and 300 s respectively (Fig. 5(a) and (b)). Interestingly, *x*Ag@TPA–CH POPs nanocomposites have better catalytic activity than *x*Ag@Py–CH POPs nanocomposites (Fig. 5(a) and (b)), this superior performance of the former assumes to the capability of tertiary amines based *x*Ag@TPA–CH POPs nanocomposites to form hydrogen bonding with phenolic hydroxyl units consequently motivates the reduction rate. Significantly, the concentration of the reducing agent ($NaBH_4$) was higher than *p*-NP therefore, these reactions supposed to follow pseudo-first-order kinetic models.[23,70,71] Realistically, the pseudo-first-order kinetic assumption expressed *via* equation of $\ln \frac{C_t}{C_0} = K_{app} \times t$ considering the apparent rate constant (K_{app}), preliminary concentration (C_0), concentration at time intervals (C_t), and time per seconds (t). Thereby, the K_{app} of 1Ag@Py–CH, 3Ag@Py–CH, 1Ag@TPA–CH and 3Ag@TPA–CH POPs nanocomposites are 4.03×10^{-3}, 9.7×10^{-3}, 6.34×10^{-3}, and 6.34×10^{-3} s^{-1}, respectively (Fig. 5(e)). On the other hand, the normalized rate constants of 1Ag@Py–CH, 3Ag@Py–CH, 1Ag@TPA–CH and 3Ag@TPA–CH POPs nanocomposites are 19.7, 48.5, 31.7, and 65.3 mg s^{-1}, respectively. From this point, we suppose, such an increase of the dipping $AgNO_3$ concentration reveals a higher deposition percentage of Ag nanoparticles onto Py–CH or even TPA–CH POPs as proven through ICP data. Therefore,

reducing efficiencies of the 3Ag@Py–CH POP toward *p*-NP is higher than 1Ag@Py–CH POPs nanocomposites. Similarly, the 3Ag@TPA–CH POP nanocomposite is better than 1Ag@TPA–CH POPs nanocomposites. The normalized rates of our *x*Ag@Py–CH and *x*Ag@TPA–CH POPs nanocomposites comparing with previously reported Ag nanoparticles decorated polymers used for heterogeneous reduction of *p*-NP exhibit promising catalytic efficiency than pyridinyl-phenanzine CMP,[4] cellulose microgels,[72] Gd-MOFs,[73] spherical COF,[74] sugar-based micro/mesoporous hypercross-linked polymers[75] and others (Fig. 5(f) and Table S2†). Further, we tested the efficiency of 1Ag@Py–CH, 1Ag@TPA–CH POP toward the reduction of *p*-chloro nitrobenzene,[76] results imply significant catalysis performances *via* these catalysts (Fig. S4†).

Importantly, turnover number (TON) and turnover frequency (TOF) for the reduction of *p*-NP using various Ag@Py–CH and Ag@TPA–CH nanocomposites reveals important insights into their catalytic performance. The TON values indicate the total number of moles of *p*-AP produced per mole of catalyst. For instance, the TON for 1Ag@Py–CH POP is recorded at 4.03 min^{-1}, while the 3Ag@Py–CH POP exhibits a higher TON of 9.70 min^{-1} (Fig. S5a†). On the other hand, the 1Ag@TPA–CH POP shows a TON of 6.34 min^{-1}, while the 3Ag@TPA–CH POP achieves a higher TON of 13.06 min^{-1} (Fig. S5b†). This suggests that increasing the Ag loading enhances catalytic efficiency. The TOF values, which measure the rate of reaction per mole of catalyst per hour, also show variability, with 1Ag@Py–CH POP showing a TOF of 366.76 h^{-1} compared to 385.73 h^{-1} for 3Ag@Py–CH POP. Otherwise, the 1Ag@TPA–CH POP exhibiting a TOF of 1119.66 h^{-1}, indicating high initial catalytic activity. However, TOF decreases over time for all samples, suggesting that although the catalysts are initially effective, their activity diminishes as the reaction progresses.

Notably, the relationship between TON and TOF reveals an exponential increase in TON over time, indicating that more product is formed as the reaction continues. This rapid conversion suggests that the catalysts are highly effective in facilitating the reduction of *p*-NP to *p*-aminophenol. Conversely, TOF values exhibit an exponential decrease with time, indicating that while initial catalytic activity is high, it declines as reactants are converted into products. This decline could be attributed to several factors, such as substrate depletion, product inhibition, or potential deactivation of active sites on the catalyst.

When comparing these results with previously reported materials in the literature (Table S3†), it is evident that our Ag@Py–CH and Ag@TPA–CH nanocomposites demonstrate competitive performance in terms of both TON and TOF. For instance, studies have shown that other metal-based catalysts often exhibit lower TOF values under similar conditions due to issues such as leaching or deactivation. The high TOF observed in our study reflects not only the effective interaction between Ag nanoparticles and the POPs but also highlights the stability and reusability of our synthesized nanocomposites.

Catalytic mechanism

For these kind of catalytic reactions, noble metals decorated polymers (nano-catalysts) provide a suitable surface for reactants (*p*-NP, and $NaBH_4$), since electron transfers facilitate the reduction processes which supposed to be modulated through these nanocatalysts. Theoretically and experimentally, the catalytic reduction of *p*-NP catalyzed by *x*Ag@Py–CH and *x*Ag@TPA–CH POPs nanocomposites, and under standard conditions could be followed the plausible mechanics as emphasized in Scheme 2. Briefly, the *p*-NP may be adsorbed onto *x*Ag@Py–CH and *x*Ag@TPA–CH POPs nanocomposites, then Ag nanoparticles react with borohydride groups to produce an Ag–H pair. After that, hydrogens move between *p*-NP and Ag–H complex thus reducing nitroaromatic units then capturing again by Ag–H units forming hydroxyl-amines. Finally, *p*-AP molecules could form due to repeated actions of Ag–H complex as shown in Scheme 2. Importantly, homogeneous distributions of Ag nanoparticles highly recommend forming Ag–H complex, moreover porous nature of Py–CH and TPA–CH POPs accelerate the mass transfer of reactants through catalytic active sites. Again, amine units of TPA–CH POP facilitate such formations of hydrogen bonding with phenolic hydroxyls hence accelerating the kinetic reduction rate of *x*Ag@TPA–CH POP nanocomposite than *x*Ag@Py–CH POP nanocomposite.

Recovery investigations

From the perspective future and practical employment of *x*Ag@TPA–CH and *x*Ag@Py–CH POP nanocomposites within catalysing reductions of *p*-NP, their stabilities consider an important parameter. Here, Ag@TPA–CH and Ag@Py–CH POPs nanocomposites were recovered and reused up to five consecutive runs for the conversion of *p*-NP into *p*-AP (Fig. 6(a)). There were no significant losses within catalytic performances of *x*Ag@TPA–CH and *x*Ag@Py–CH POP nanocomposites within increasing cycle number. We have conducted ICP tests to measure the Ag content in the supernatant following the completion of our recycling experiments. The results indicate

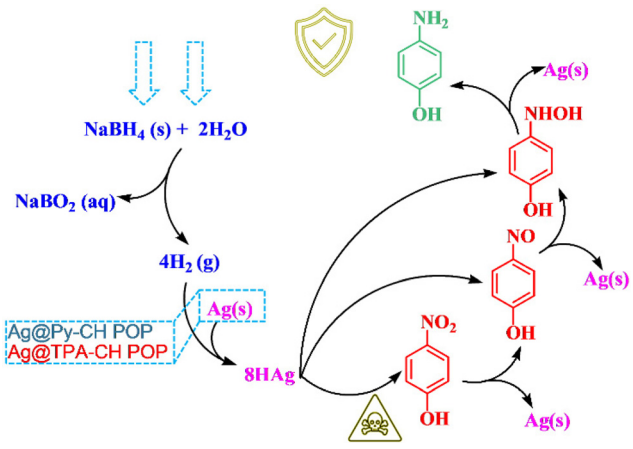

Scheme 2 The proposed reduction mechanism of *p*-NP catalyzed Ag nanoparticles decorated CH-POPs nanocomposites.

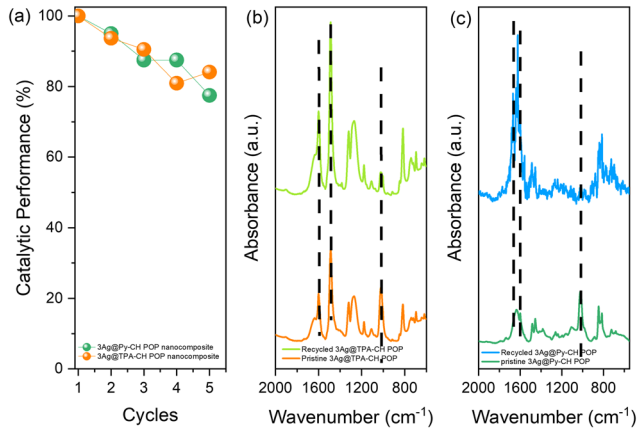

Fig. 6 Catalytic performance within five cycles of *p*-NP reduction up on using 3Ag@Py–CH POP and 3Ag@TPA–CH POP (a) FTIR fresh and recovered 3Ag@Py–CH POP (b), FTIR of fresh and recovered 3Ag@TPA–CH POP (c).

that no Ag nanoparticles were detected in the supernatant, suggesting that leaching is not a significant factor contributing to the observed decrease in catalytic performance. Instead, we believe that the reduction in catalytic activity is primarily attributed to minimal sample loss that may occur between cycling processes. These results elucidate that our nano-catalysts developed by the current study (Ag@TPA–CH and Ag@Py–CH POP nanocomposites) exhibit outstanding stabilities within several recycles. Furthermore, FTIR signals of the Ag@TPA–CH and Ag@Py–CH POP nanocomposites after recycling tests exhibit very little shifts compared with fresh moieties (Fig. 6(b)–(c)). These important results assume the chemical stabilities of Ag@CH POPs nanocomposites for their futuristic usage.

Conclusions

We synthesized CH-based POPs (Py–CH POP, and TPA–CH POP) *via* simple Friedel–Crafts alkylation. Further, we characterized these novel POPs using FTIR, solid state NMR, TGA, BET methodologies, XPS, SEM, and TEM which emphasized the outstanding physical and chemical properties of these novel materials. Furthermore, hydroxyl units based Py–CH, and TPA–CH POPs facilitated capturing of Ag^{+} ions achieving preparations of Ag@Py–CH, and Ag@TPA–CH POPs nanocomposites (green reduction). The Ag@Py–CH, and Ag@TPA–CH POPs nanocomposites showed efficient catalytic performances within disposal of hazardous pollutants. The Ag@Py–CH, and Ag@TPA–CH POPs nanocomposites provided higher normalized catalytic reduction rates of *p*-NP up to 48.5, and 65.3 mg s^{-1} respectively comparable with reported catalysts used for this regard. Further, Ag@ Py–CH, and Ag@TPA–CH POPs nanocomposites displayed efficient recyclability without considerable losses of performance. Furthermore, this paper not only offers new substrates used as high rated catalysts toward *p*-NP reductions but also exhibits a new strategy for simple and green decoration of porous polymers with Ag nanoparticles for various life applications.

Data availability

The data supporting this article have been included as part of the ESI.†

Conflicts of interest

There are no conflicts to declare.

Acknowledgements

This study was supported financially by the National Science and Technology Council, Taiwan, under contracts NSTC 113-2223-E-110-001 and 113-2221-E-110 -012 -MY3.

References

1 T. Zhou, Z. Liu and T. Yu, *Ind. Eng. Chem. Res.*, 2024, **63**, 12806–12814.
2 T. Ma, X. Tan, Q. Zhao, Z. Wu, F. Cao, J. Liu, X. Wu, H. Liu, X. Wang and H. Ning, *Ind. Eng. Chem. Res.*, 2019, **59**, 129–136.
3 Y. Li, J. Shen, Y. Hu, S. Qiu, G. Min, Z. Song, Z. Sun and C. Li, *Ind. Eng. Chem. Res.*, 2015, **54**, 9750–9757.
4 M. G. Kotp, A. F. M. El-Mahdy, T.-L. Yang and S.-W. Kuo, *Microporous Mesoporous Mater.*, 2022, **331**, 111669.
5 D. S. Rana, S. Kalia, R. Kumar, N. Thakur, R. K. Singh and D. Singh, *Environ. Nanotechnol., Monit. Manage.*, 2022, **18**, 100724.
6 B. Liu, S. Li, Y. Zhao, W. Wu, X. Zhang, X. Gu, R. Li and S. Yang, *J. Hazard. Mater.*, 2010, **176**, 213–219.
7 O. Güven, S. Demirci, S. D. Sütekin, B. Ari and N. Sahiner, *Radiat. Phys. Chem.*, 2022, **198**, 110217.
8 B. Jiang, A. Li, C. Shuang, Y. Tan, Y. Pan and F. Liu, *Chemosphere*, 2022, **305**, 135400.
9 Y. Tan, W. Chen, G. Liao, X. Li, J. Wang, Y. Tang and L. Li, *Appl. Catal., B*, 2022, **306**, 121133.
10 R. Manno, V. Sebastian, S. Irusta, R. Mallada and J. Santamaria, *Catal. Today*, 2021, **362**, 81–89.
11 S.-X. Li, F.-Y. Zheng, X.-L. Liu, F. Wu, N.-S. Deng and J.-H. Yang, *Chemosphere*, 2005, **61**, 589–594.
12 L. Song, L. Shu, Y. Wang, X.-F. Zhang, Z. Wang, Y. Feng and J. Yao, *Int. J. Biol. Macromol.*, 2020, **143**, 922–927.
13 Z. Qu, X. Xu, H. Ren, T. Sun, L. Huang and Z. Gao, *J. Environ. Chem. Eng.*, 2022, **10**, 108185.
14 P. Zhao, X. Feng, D. Huang, G. Yang and D. Astruc, *Coord. Chem. Rev.*, 2015, **287**, 114–136.
15 S. Uehara, N. Inomata, A. Suzuki, M. Matsuura and M. Aihara, *J. Dermatol.*, 2014, **41**, 560–561.

16 W.-C. Chen, Y.-T. Liu and S.-W. Kuo, *Polymers*, 2020, **12**, 2151.
17 Y.-C. Huang, W.-C. Chen and S.-W. Kuo, *Macromolecules*, 2022, **55**, 8918–8930.
18 T.-C. Chou and S.-W. Kuo, *Macromolecules*, 2024, **57**, 5958–5970.
19 C.-F. Wang, Y.-T. Wang, P.-H. Tung, S.-W. Kuo, C.-H. Lin, Y.-C. Sheen and F.-C. Chang, *Langmuir*, 2006, **22**, 8289–8292.
20 W.-C. Chen, M. M. Ahmed, C.-F. Wang, C.-F. Huang and S.-W. Kuo, *Polymer*, 2019, **185**, 121940.
21 D. Jain and G. Madras, *Ind. Eng. Chem. Res.*, 2017, **56**, 2008–2024.
22 F. Shao, X. Wang, Z. Zhao, Z. Wei, X. Zhong, Z. Yao, S. Deng, S. Wang, H. Wang and A. Li, *Ind. Eng. Chem. Res.*, 2022, **61**, 3474–3482.
23 M. M. Ayad, W. A. Amer and M. G. Kotp, *Mol. Catal.*, 2017, **439**, 72–80.
24 M. M. Ayad, W. A. Amer, M. G. Kotp, I. M. Minisy, A. F. Rehab, D. Kopecký and P. Fitl, *RSC Adv.*, 2017, **7**, 18553–18560.
25 T.-H. Chang, K.-W. Chuang, Y.-C. Chang and C.-M. Chou, *Mater. Chem. Phys.*, 2022, **280**, 125823.
26 N. T. L. Chi, M. Narayanan, A. Chinnathambi, C. Govindasamy, B. Subramani, K. Brindhadevi, T. Pimpimon and S. Pikulkaew, *Environ. Res.*, 2022, **208**, 112684.
27 M. Rahimi, E. B. Noruzi, E. Sheykhsaran, B. Ebadi, Z. Kariminezhad, M. Molaparast, M. G. Mehrabani, B. Mehramouz, M. Yousefi and R. Ahmadi, *Carbohydr. Polym.*, 2020, **231**, 115696.
28 D.-H. Yang, Y. Tao, X. Ding and B.-H. Han, *Chem. Soc. Rev.*, 2022, **51**, 761–791.
29 Z. Zhang, J. Jia, Y. Zhi, S. Ma and X. Liu, *Chem. Soc. Rev.*, 2022, **51**, 2444–2490.
30 S. Wang, H. Li, H. Huang, X. Cao, X. Chen and D. Cao, *Chem. Soc. Rev.*, 2022, **51**, 2031–2080.
31 C.-W. Hsiao, A. M. Elewa, M. G. Mohamed, M. G. Kotp, M. M.-C. Chou and S.-W. Kuo, *Colloids Surf., A*, 2024, 134658.
32 T.-L. Lee, A. M. Elewa, M. G. Kotp, H.-H. Chou and A. F. M. El-Mahdy, *Chem. Commun.*, 2021, **57**, 11968–11971.
33 M. G. Mohamed, A. F. M. El-Mahdy, M. G. Kotp and S.-W. Kuo, *Mater. Adv.*, 2022, **3**, 707–733.
34 M. G. Kotp, N. L. Torad, H. Nara, W. Chaikittisilp, J. You, Y. Yamauchi, A. F. M. El-Mahdy and S.-W. Kuo, *J. Mater. Chem. A*, 2023, **11**, 15022–15032.
35 A. F. M. El-Mahdy, J. Lüder, M. G. Kotp and S.-W. Kuo, *Polymers*, 2021, **13**, 1385.
36 M. G. Kotp, S. U. Sharma, J.-T. Lee, A. F. M. El-Mahdy and S.-W. Kuo, *J. Taiwan Inst. Chem. Eng.*, 2022, **134**, 104310.
37 M. G. Kotp and S.-W. Kuo, *Polymers*, 2024, **13**, 1759.
38 A. O. Mousa, M. G. Mohamed, Z.-I. Lin, C.-H. Chuang, C.-K. Chen and S.-W. Kuo, *Eur. Polym. J.*, 2023, **196**, 112254.
39 A. O. Mousa, M. G. Mohamed, Z.-I. Lin, C.-H. Chuang, C.-K. Chen and S.-W. Kuo, *J. Taiwan Inst. Chem. Eng.*, 2024, **157**, 105448.
40 A. O. Mousa, S. U. Sharma, S. V. Chaganti, T. H. Mansoure, P. N. Singh, M. Ejaz, C.-H. Chuang, J.-T. Lee, S.-W. Kuo and M. G. Mohamed, *J. Power Sources*, 2024, **608**, 234624.
41 A. O. Mousa, Z.-I. Lin, C.-H. Chuang, C.-K. Chen, S.-W. Kuo and M. G. Mohamed, *Int. J. Mol. Sci.*, 2023, **24**, 8966.
42 A. O. Mousa, C.-H. Chuang, S.-W. Kuo and M. G. Mohamed, *Int. J. Mol. Sci.*, 2023, **24**, 12371.
43 M. G. Kotp and S.-W. Kuo, *Mater. Today Chem.*, 2024, **41**, 102299.
44 M. G. Kotp, A. F. M. El-Mahdy, M. M. Chou and S.-W. Kuo, *New J. Chem.*, 2024, **48**, 14435–14443.
45 J.-S. M. Lee and A. I. Cooper, *Chem. Rev.*, 2020, **120**, 2171–2214.
46 K. Liang, L. Lu, X. Liu, D. Yang, S. Wang, Y. Gao, H. Alhumade, H. Yi and A. Lei, *ACS Catal.*, 2021, **11**, 14892–14897.
47 H. Qiu, B. Shuai, Y.-Z. Wang, D. Liu, Y.-G. Chen, P.-S. Gao, H.-X. Ma, S. Chen and T.-S. Mei, *J. Am. Chem. Soc.*, 2020, **142**, 9872–9878.
48 M. G. Kotp, A. M. Elewa, A. F. M. El-Mahdy, H.-H. Chou and S.-W. Kuo, *ACS Appl. Energy Mater.*, 2021, **4**, 13140–13151.
49 M. Ahmed, M. G. Kotp, T. H. Mansoure, R.-H. Lee, S.-W. Kuo and A. F. M. El-Mahdy, *Microporous Mesoporous Mater.*, 2022, **333**, 111766.
50 M. G. Kotp, J. Lüder, S.-W. Kuo and A. F. M. El-Mahdy, *Mater. Adv.*, 2024, **5**, 4142–4150.
51 M. G. Kotp, S.-W. Kuo and A. F. M. El-Mahdy, *Colloids Surf., A*, 2024, 133210.
52 M. G. Kotp, C.-L. Chang and A. F. El-Mahdy, *J. Water Process Eng.*, 2023, **53**, 103675.
53 F. Khosravi, M. Gholinejad, J. M. Sansano and R. Luque, *Mol. Catal.*, 2022, **522**, 112199.
54 A. O. Mousa, M. G. Mohamed, C.-H. Chuang and S.-W. Kuo, *Polymers*, 2023, **15**, 1891.
55 J. Wang, L. Zhang, Y. Jing, W. Huang and X. Zhou, *Tetrahedron Lett.*, 2009, **50**, 4978–4982.
56 S. Che and L. Fang, *Chem*, 2020, **6**, 2558–2590.
57 S. Isikli, M. Lecea, M. Ribagorda, M. C. Carreño and R. Díaz, *Carbon*, 2014, **66**, 654–661.
58 H.-L. Cao, H.-B. Huang, Z. Chen, B. Karadeniz, J. Lü and R. Cao, *ACS Appl. Mater. Interfaces*, 2017, **9**, 5231–5236.
59 S. Ren, R. Dawson, D. J. Adams and A. I. Cooper, *Polym. Chem.*, 2013, **4**, 5585–5590.
60 M. G. Kotp, N. L. Torad, J. Lüder, A. El-Amir, W. Chaikittisilp, Y. Yamauchi and A. F. M. El-Mahdy, *J. Mater. Chem. A*, 2023, **11**, 764–774.
61 X.-H. Du, Z. Jiang, Z. Liu and C. Xu, *Microporous Mesoporous Mater.*, 2022, **332**, 111711.
62 S. S. Chu, G. Jeffrey and T. Sakurai, *Acta Crystallogr.*, 1962, **15**, 661–671.
63 G. Das, T. Skorjanc, S. K. Sharma, T. Prakasam, C. Platas-Iglesias, D. S. Han, J. Raya, J. C. Olsen, R. Jagannathan and A. Trabolsi, *ChemNanoMat*, 2018, **4**, 61–65.
64 T.-K. Huang, T.-H. Cheng, M.-Y. Yen, W.-H. Hsiao, L.-S. Wang, F.-R. Chen, J.-J. Kai, C.-Y. Lee and H.-T. Chiu, *Langmuir*, 2007, **23**, 5722–5726.

65 M. Capocelli, M. Prisciandaro, A. Lancia and D. Musmarra, *Chem. Eng. J.*, 2014, **254**, 1–8.
66 Q. Yue, J. Li, Y. Zhang, X. Cheng, X. Chen, P. Pan, J. Su, A. A. Elzatahry, A. Alghamdi and Y. Deng, *J. Am. Chem. Soc.*, 2017, **139**, 15486–15493.
67 P.-C. Chen, G. Liu, Y. Zhou, K. A. Brown, N. Chernyak, J. L. Hedrick, S. He, Z. Xie, Q.-Y. Lin and V. P. Dravid, *J. Am. Chem. Soc.*, 2015, **137**, 9167–9173.
68 M. Li and G. Chen, *Nanoscale*, 2013, **5**, 11919–11927.
69 S. Bae, S. Gim, H. Kim and K. Hanna, *Appl. Catal., B*, 2016, **182**, 541–549.
70 J. Sun, Y. Fu, G. He, X. Sun and X. Wang, *Catal. Sci. Technol.*, 2014, **4**, 1742–1748.
71 J. Du and Z. Xia, *Anal. Methods*, 2013, **5**, 1991–1995.
72 Y. Han, X. Wu, X. Zhang, Z. Zhou and C. Lu, *ACS Sustainable Chem. Eng*, 2016, **4**, 6322–6331.
73 Y.-P. Wu, G.-W. Xu, W.-W. Dong, J. Zhao, D.-S. Li, J. Zhang and X. Bu, *Inorg. Chem.*, 2017, **56**, 1402–1411.
74 N. Wang, F. Wang, F. Pan, S. Yu and D. Pan, *ACS Appl. Mater. Interfaces*, 2021, **13**, 3209–3220.
75 Q. Yin, Q. Chen, L.-C. Lu and B.-H. Han, *Beilstein J. Org. Chem.*, 2017, **13**, 1212–1221.
76 A. Monga and B. Pal, *RSC Adv.*, 2015, **5**, 39954–39963.